Overcoming The Low Initial Coulombic Efficiency of Si Anodes Through Prelithiation in All-solid-state Batteries

So-Yeon Ham[1], Elias Sebti[2], Ashley Cronk[1], Tyler Pennebaker[2], Grayson Deysher[1], Yu-Ting Chen[1], Jin An Sam Oh[3], Jeong Beom Lee[4], Min Sang Song[4], Phillip Ridley[5], Darren H. S. Tan[5], Raphaële J. Clément[2], Jihyun Jang[7,*], and Ying Shirley Meng[5,6,*]

[1]*Materials Science and Engineering Program, University of California San Diego, La Jolla, 92093, United States.*
[2]*Materials Department and Materials Research Laboratory, University of California, Santa Barbara, California 93106, United States.*
[3]*Insitute of Materials, Research, and Engineering, Agency of Science, Technology, and Research (A*STAR), Singapore*
[4]*LG Energy Solution. Ltd., LG Science Park, Magokjungang 10-ro, Gangseo-gu, Seoul 07796, Korea.*
[5]*Department of NanoEngineering, University of California San Diego, La Jolla, California 92093, United States.*
[6]*Pritzker School of Molecular Engineering, University of Chicago, Chicago, Illinois 60637, United States.*
[7]*Department of Chemistry, Sogang University, Seoul, 04107, Republic of Korea*
**Correspondence to: jihyunjang@sogang.ac.kr, shirleymeng@uchicago.edu*

Keywords

All-solid-state battery, Prelithiation, Si anodes, Initial Coulombic efficiency improvement

Abstract

All-solid-state batteries using Si as the anode have shown promising performance without continual solid-electrolyte interface (SEI) growth. However, the low initial Coulombic efficiency (ICE) of Si limits their energy density. In this work, a prelithiation strategy was adopted to improve the ICE and conductivity of Si all-solid-state cells. Lithiated Si anodes were examined in symmetric-, half-, and full-cell configurations to understand the cell-level improvement. A full cell comprising a Li_1Si anode achieved over 95% of ICE when paired with a lithium cobalt oxide (LCO) cathode. Additionally, a comparison of cells containing either a lithium nickel manganese cobalt oxide (NCM) or LCO cathode paired with either Si or Li_xSi at the anode revealed performance improvements with Si prelithiation only in anode-limited cases. Rate and long-term cycling capabilities were evaluated for Si- and Li_1Si-containing cells, showing higher discharge capacities at all rates for Li_1Si than Si. With Li_1Si, 73.8% capacity retention was achieved after 1000 cycles, a 15% improvement when compared to a pure Si anode. With Li_1Si, a high areal capacity of up to 10 mAh cm^{-2} was attained using a dry-processed LCO cathode film, suggesting that the prelithiation method may be suitable for high loading next-generation all-solid-state batteries.

1. Introduction

All-solid-state batteries (ASSBs) have drawn considerable attention as safer and potentially more energy-dense devices as compared to conventional liquid cells. Achieving high energy density ASSBs depends on the development of high-capacity electrodes in a solid-state architecture.[1,2] On the anode side, potential candidate materials or architectures include Li metal,[3–6] anode-free,[7] and alloy-type anodes such as Li-Si,[8,9] Li-In,[10–13] Li-Sn,[14] Li-Al,[15,16] Li-Sb,[17] and Li-Mg.[18] However, high specific capacity and low propensity for Li dendrite growth and cell shorting make alloy-type anodes the most promising for next-generation ASSBs.

Si has been extensively studied in lithium-ion batteries (LIBs) for decades. Many reports have suggested that the use of pure Si as the anode is impractical due to its poor interfacial stability with liquid electrolytes and pulverization during cycling.[19,20] However, a recent study demonstrated the use of a 99.9 wt. % micro-silicon (µSi) anode in combination with an argyrodite solid electrolyte (Li_6PS_5Cl) to produce an ASSB with a high areal current density and high areal loadings.[21] The successful use of µSi as an anode was attributed to passivation of the sulfide electrolyte-Si interface, limiting the growth of a poorly-conducting solid-electrolyte interphase (SEI).

Although Si-based all-solid-state cells with a passivating SEI and a high energy density have already been demonstrated, further performance improvements can be achieved, including increases in the initial Coulombic efficiency (ICE), electronic conductivity, and Li^+ diffusivity (**Figure 1**). Notably, prelithiation of Si, which has traditionally been implemented in LIBs,[22] could be a good approach to enable such improvements.

One of the well-established prelithiation methods is electrochemical prelithiation.[23–26] In this approach, a Si electrode is lithiated by building an electrochemical cell comprising a Li metal counter electrode and a non-aqueous electrolyte. The redox potential difference of the two electrodes results in spontaneous lithiation of Si and SEI formation. However, the extent of "electrochemical" prelithiation must be well controlled, since insufficient lithiation cannot improve the ICE due to remaining Li trapping sites, while over-lithiation could start the lithium

plating on the anode surface.[27] Due to the high chemical reactivity of Li, one of the challenges to implement the successful prelithiation lies in finding the stable prelithiation reagents (Li source). As such, Cao *et al.* introduced a polymer to protect the Li source, where the metallic Li source for prelithiation was shielded by the polymer before made into the full cell.[28] More commercially viable option of prelithiation reagent is the stabilized lithium metal powder (SLMP). Ai *et al.* developed a solution process to coat SLMP on anode material, where both graphite/NMC and SiO/NMC full cells exhibited 31% higher ICE after prelithiation of the anodes.[29] Forney *et al.* deposited SLMP on a Si – carbon nanotube (CNT) anode and used a mechanical press to apply a pressure of 100-300 PSI to the stack for 30-60 s to crack the electronically insulating Li_2CO_3 coating of SLMP and facilitate the prelithiation process.[30] Another study showed that mere contact between passivated Li metal powder (PLMP) and a Si/graphite electrode could induce prelithiation.[31]

The first Si-based all-solid state battery with prelithiation of the Si anode was recently reported,[32] where prelithiation of Si was completed by ball-milling with Li metal in anhydrous hexane. Starting from the prelithiated Si, further mechanochemical milling was needed to mix the Li_xSi active material, the solid electrolyte, and the carbon additive to form the composite anode. The Li_xSi composite electrode was paired with a sulfur cathode and the full cell demonstrated a stable capacity for over 500 cycles. While such performance is impressive, this work required an extra high energy ball-milling step in organic solvent to prelithiate the Si, adding complexity to the ASSB fabrication process.

Despite extensive research efforts over the past few years, prelithiation of Si during cell fabrication without involving any electrolyte or carbon has yet to be demonstrated. We introduce here a simple pressure-induced prelithiation strategy for Si anodes during ASSB fabrication. The prelithiated Si anode was characterized using solid-state nuclear magnetic resonance (ssNMR). The performance of our prelithiated Si anode was evaluated in symmetric-, half-, and full-cells. The effectiveness of the prelithiation approach was further assessed using two different cathodes, NCM811 and LCO, to elucidate the limiting component of the ASSB. Finally, a cell of prelithiated Si paired with LCO showed a high ICE of over 95% with a stable cyclability for 1000 cycles at 5 mA cm^{-2} current density.

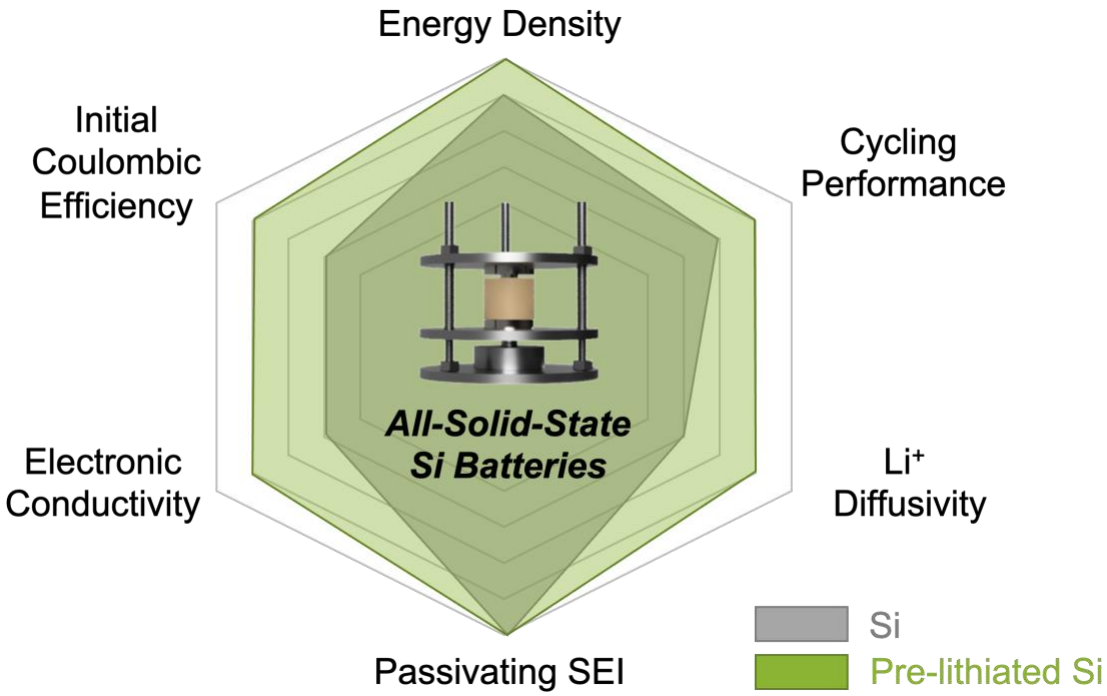

Figure 1. A radar comparison chart of Si (gray shade) and prelithiated Si (green shade) anodes for various electrochemical properties and battery performance metrics.

2. Results and Discussion

2.1 Pressure-induced prelithiation of Si

Prelithiation of Si was conducted via a simple mixing process coupled with a pressurizing step. In this work, an anode composed of vortex-mixed μSi and SLMP was introduced for the first time in an ASSB. Different amounts of SLMP were mixed with μSi powder to produce Li_xSi alloys with a molar ratio x = 0.25, 1, and 2 (e.g., $Li_{0.25}Si$, Li_1Si and Li_2Si). We note that those x values assume that the SLMP in μSi powders have fully reacted. The morphology of μSi and SLMP was investigated with scanning electron microscopy (SEM), indicating a particle size distribution of 2 - 5 μm for μSi and 10 - 60 μm for spherical SLMP (**Figure S1a, b**). From **Figure 2a**, we find that Si and Li domains in the final Li_1Si powder retain the morphology of the precursor particles. The absence of energy dispersive X-ray spectroscopy (EDS) signal from spherical regions within the Li_1Si powder sample allow their assignment to pure lithium metal due to the low energy of the Li X-ray transition (**Figure 2a**). In **Figure 2b**, a cross-sectional focused ion beam scanning electron microscopy (FIB-SEM) image was obtained on a 200 MPa pressed Li_1Si pellet. The pressed Li_1Si sample exhibits two types of domains: 1) regions comprised of distinct μSi and Li sub-domains, and 2) regions where the μSi and Li precursors alloyed to form a new chemical composition. In the first type of domain, Li sub-domains are sandwiched between μSi domains, resulting in a different morphology from the SLMP precursor powder. Again, no EDS signal could be detected

from those Li-rich sub-domains. The second type of domain has an entirely different morphology from the pristine μSi and SLMP powders, that is more comparable to charged (lithiated) Si where the gap between individual Si particle disappears and large Si blocks are formed instead. Additionally, Si EDS signal can be detected from those regions. All in all, this analysis indicates that after pressing at 200 MPa for 30 s, the Li_1Si anode exhibits unreacted Li and μSi, as well as a Li-Si alloy phase.

To better understand the extent of alloy formation from pressurizing SLMP and μSi precursors, ^{7}Li ssNMR was used to probe the chemical state of bulk lithiated Si. ssNMR is crucial here, as lithiated Si is amorphous and cannot be studied using standard diffraction methods. ^{7}Li ssNMR, on the other hand, is sensitive to crystalline and amorphous phases alike and allows to distinguish and, in theory, quantify Li metal (265 ppm)[33] from the Li-Si alloy (broad signal centered around 0 ppm)[31] as their respective signals are well resolved. However, the penetration of the radiofrequency (RF) pulses used to excite the nuclear spins in a ssNMR measurement into metallic samples is limited and inversely proportional to the square root of the electronic conductivity. This results in a so-called "skin depth" of around 7.4 μm for Li metal (with an electronic conductivity of 1.1 x 10^7 S/cm[34]) under the chosen experimental conditions,[35] which is lower than the radius of some pristine SLMP particles (5 – 30 μm) and thus leads to an underestimation of the amount of metallic Li in the sample. The Li-Si alloy phases that form in the samples under consideration are many orders of magnitude less conductive than Li metal, as will be discussed in the next section, and their minimum skin depth of ~570 μm (calculated based on Li_2Si electronic conductivity) ensures that such regions can be probed quantitatively with ^{7}Li ssNMR. We note, however, that the Li-Si alloy signal likely overlaps with minor diamagnetic impurity phases that inevitably form at the surface of metallic Li (even when air/moisture exposure was avoided by handling the samples in the glovebox at all times), including LiOH and Li_2CO_3 resonating at ~0 ppm.[36] In **Figure 2c**, ^{7}Li ssNMR was conducted on several SLMP + μSi samples subjected to pressures varying from 0 to 400 MPa for 30 s to 3 minutes to determine the conditions under which maximum Si prelithiation is achieved. Given that the size distribution of metallic Li sub-domains in the pressed samples is on par with the particle size distribution of the SLMP precursor, the relative amount of Li metal detected by ^{7}Li ssNMR follows the same trend as the actual amount of metallic Li in the samples of interest to this work, despite skin depth issues. This allows us to use the relative integrated intensity of the Li metal and Li-Si alloy signals in the ^{7}Li ssNMR spectra to follow the incorporation of Li into Si as a function of sample processing conditions. The impact of ssNMR signal (T_2*) relaxation during data acquisition was accounted for in the quantification of the observable Li signals (see results in **Table S1)** for all samples except the unpressed Li_1Si for which a T_2* measurement could not be conducted due to sample evolution in the spectrometer. The unpressed Li_1Si sample contains the most Li metal and a smaller fraction of the Li-Si phase, with the 0 ppm resonance accounting for 27.8 % of the total ^{7}Li ssNMR signal intensity. Despite the lack of T2* adjustment for this sample, these results are expected to hold as the changes in Li molar % from T2* adjustment of Li metal or diamagnetic phases for other samples are smaller than 1%. Conversely, pressed Li_1Si samples exhibit > 92% of the total ^{7}Li signal intensity at 0 ppm, indicating the presence of a major Li-Si alloy phase. The relative intensity of the 0 ppm signal as compared to the Li metal signal increases with higher pressure and longer pressing time, indicating an increased fraction of Li-Si alloy in the sample. For example, applying 200 MPa of pressure for 3 min (green) leads to greater Li incorporation into the Si phase than applying the same amount of pressure for 30 s (blue), as evidenced by the 98.2 and 92.9% of the total ^{7}Li ssNMR signal intensity present at 0 ppm for these two samples, respectively. Those results

indicate that a Li-Si alloy can be formed by pressurizing the SLMP and μSi precursor powders in the absence of electrolyte, demonstrating that the latter is not required to facilitate the alloying reaction unlike previously thought.[37] Interestingly, unpressed Li_xSi samples evolve over the course of the ssNMR measurements, while the composition of pressed samples remains stable. This is shown in **Figure S2**, where ^{7}Li ssNMR spectra collected on four different Li_xSi samples (Li_1Si and Li_2Si non-pressurized and pressurized at 200 MPa for 30 s) before, during, and after a T_2* relaxation time measurement, are compared. For the unpressed samples, the 0 ppm signal increases over the course of the measurement, indicating that Li-Si alloying is taking place over time. On the other hand, the spectra of the pressed samples do not evolve because Si has already been lithiated at 200 MPa and is stable under ambient conditions.

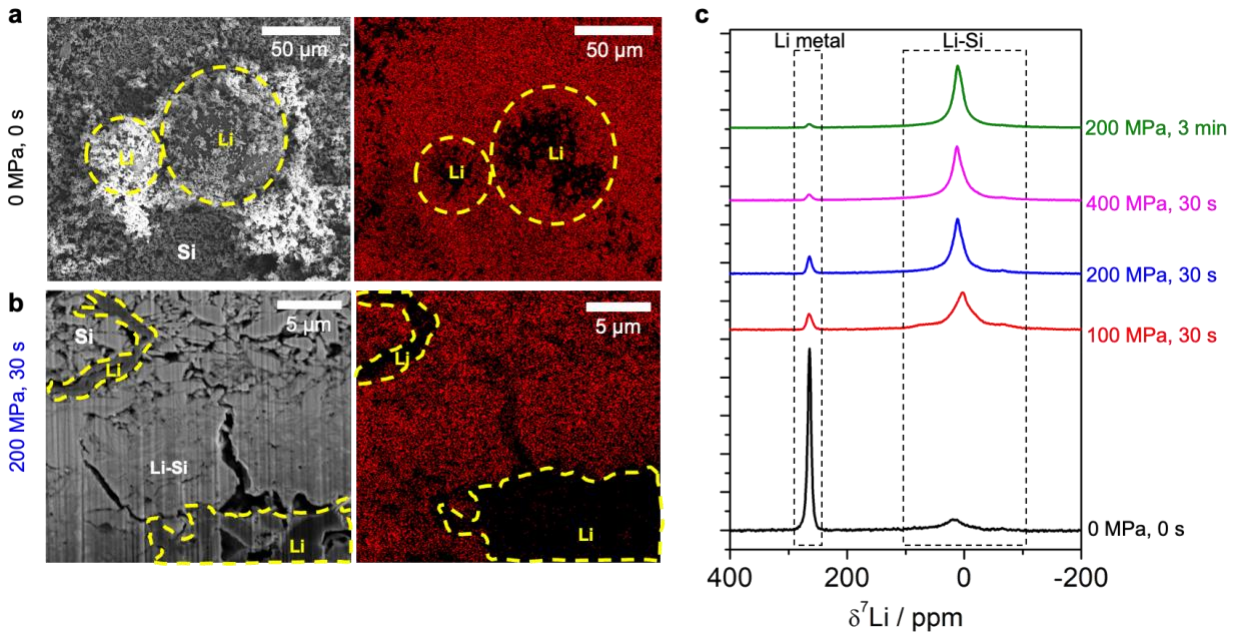

Figure 2. a) FIB/SEM cross-sectional image of non-pressed (0 MPa, 0 s) and b) pressed (200 MPa, 30 s) Li_1Si pellet before cycling. c) ^{7}Li NMR spectra of Li_1Si with different pressure and time.

2.2 Electrochemical comparison of Li_xSi in symmetric, half, and full cells

Although Si is a semiconductor, its low electronic conductivity (in the range of 10^{-4} S cm^{-1}), results in a large overpotential within the cell. The conventional way to overcome this barrier is to add carbon or some conductive agent, creating a silicon composite anode. However, the addition of Li into silicon could be another way to increase the electronic conductivity of Si dramatically. **Figure 3a** shows that as Li content increases, the Li_xSi electronic conductivity increases from 10^{-4} (Li_0Si) to 10 S cm^{-1} (Li_2Si). Since pressure-induced lithiation of Si was proven to be an effective approach from the previous section, we evaluated the electrochemical properties of Li_xSi in the cell configuration of symmetric, half and full cells.

In **Figure 3b**, the plating and stripping of Li_xSi symmetric cells were conducted to evaluate the overpotential of each cell. The overpotentials of cells decrease with more Li in Si, which is

consistent with higher electronic conductivity of higher Li content Si from **Figure 3a**. The high electronically conductive Li_2Si symmetric cell had much smaller overpotential than $Li_{0.25}Si$ symmetric cell.

Electrochemical impedance spectroscopy (EIS) was used to evaluate the resistance of Li_xSi symmetric cells before and after lithiation and delithiation respectively in **Figure 3c** and **Figure 3d**. Before plating and stripping, the resistance of $Li_{0.25}Si$ is higher than that of Li_1Si or Li_2Si. The resistance value slightly decreased after plating and stripping, maintaining the trend of higher Li content in Si resulting in lower impedance. The resistance values of Li_1Si and Li_2Si before and after plating were comparable to the ionic conductivity of the sulfide electrolyte Li_6PS_5Cl (LPSCl) electrolyte layer, indicating Li_1Si nor Li_2Si is not a dominant component of the cell resistance.

Figure 3e shows the half-cell configuration of Li_xSi with Li metal. All Li_xSi was first lithiated and then delithiated after 0 V vs. Li/Li^+. Interestingly, all Li_xSi exhibited similar overpotential during the lithiation, indicating that Li reacting with Si into Li_xSi requires a similar amount of overpotential. The non-prelithiated Si clearly showed the higher overpotential when it was first lithiated due to its poorer electronic conductivity. However, the overpotential difference is prominently different in all Li_xSi. For instance, Li_2Si overpotential was 0.2 V, whereas Si overpotential was much higher and it rapidly increased as Si was more delithiated. This indicates that it is harder to delithiate Li_xSi depending on how much Li is in Si. In addition, the irreversible capacity from the initial lithiation and delithiation was observed in Li_xSi paired with Li counter electrode. There are two sources of irreversible capacity during the first cycle; one is the electrolyte decomposition on the interface and the other is Li trapped inside Si,[21] which are successfully compensated for by our prelithiation strategy.

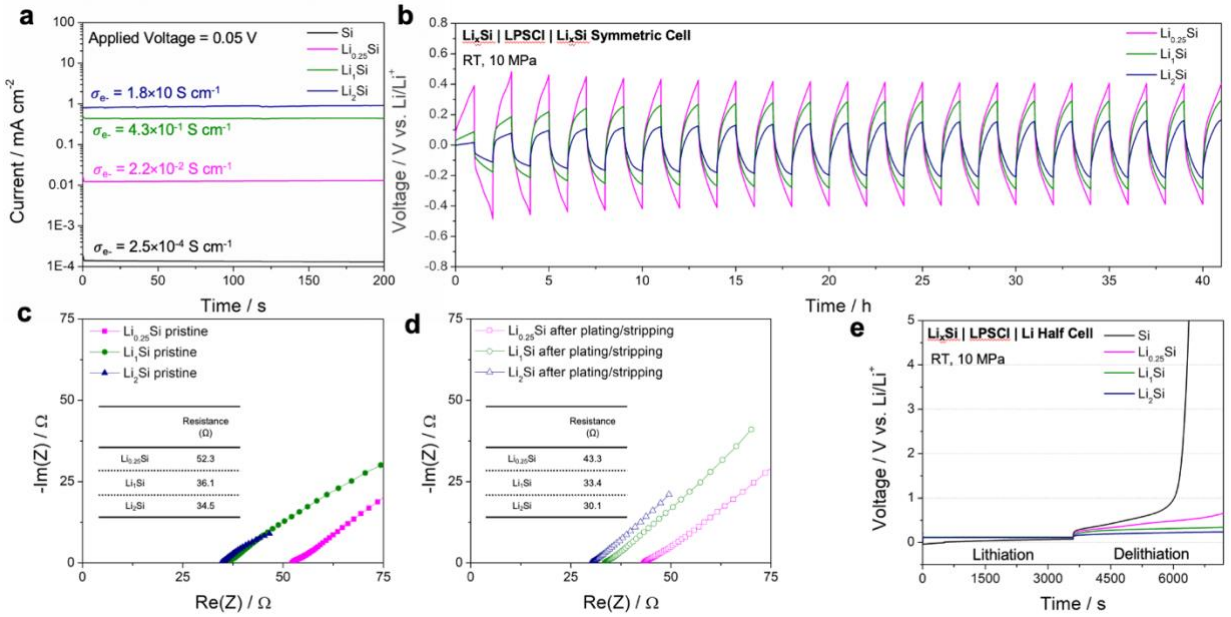

Figure 3. a) Electronic conductivity of Si and vortex mixed Li_1Si using direct current polarization. b) Plating and stripping of Li_xSi (x=0.25, 1, 2) for 15 cycles at 0.2 mA cm^{-2}. c) EIS measurement of Li_xSi symmetric cell before plating/stripping. d) EIS measurement of Li_1Si symmetric cell after plating/stripping at 0.2 mA cm^{-2} and 1.0 mA cm^{-2}. e) Lithiation/delithiation of Li_xSi half-cell with different lithiation states.

In **Figure 4a**, full cells with the following configuration, Li_xSi | LPSCl | LCO, were fabricated and cycled at C/20 to study the effect of various prelithiation amounts in Si, which was to evaluate the performance with limited lithium inventory. Although the charge capacities of all Li_xSi were similar, the discharge capacity of Li_xSi showed significant differences. This result is also reflected in the half-cell configuration in **Figure 3e**, where lithiation of Si (charging) is comparable but delithiation of Si (discharging) shows a dramatic change in ICE. The ICE of the LCO-Si full cell was 78.3% whereas the ICE of LCO-Li_1Si and LCO-Li_2Si was increased to over 95% (Figure 4b).

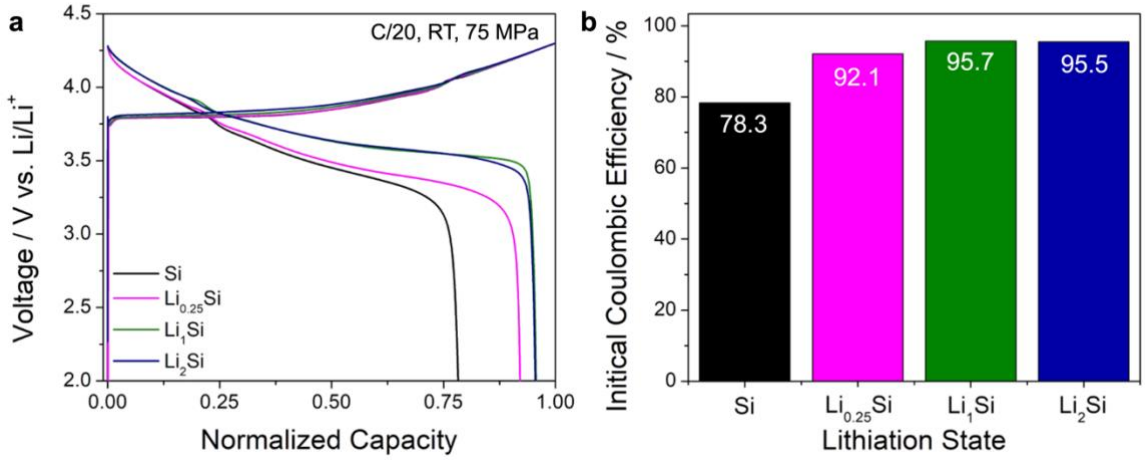

Figure 4. a) 1st cycle voltage curve of Li_xSi full cells with different lithiation states. LCO | LPSCl | Li_xSi cells were cycled at room temperature and 75 MPa. b) ICE trend of Li_xSi (x=0, 0.25, 1, 2).

2.3 Cathode limiting or anode limiting: NCM811/LCO and Si/Li_1Si

Two different cathodes were paired with Si and Li_xSi to elucidate the limiting component of the system (**Figure 5**). Based on the half-cell data of each component with a Li counter electrode, we can assume ICE of **NCM** as 75%, Si as 80%, and LCO as 95% (**Figure S3**). For NCM and LCO cathode paired with Si and lithiated Si, we can assume four cases. (**Figure 5a**) For the NCM/Si full-cell, the overall ICE is limited by the ICE of NCM, while the Si ICE determines the ICE of the LCO/Si full-cell. Therefore, pairing NCM with lithiated Si with excess Li on the anode side, the cell will still be limited by the ICE of NCM and will be unable to utilize the excess Li. However, by pairing LCO with lithiated Si, we can utilize the excess Li during the first discharge, and the cell can reach the ICE limit of LCO yielding 95%. Therefore, Case 1 (NCM/Si) and 3 (NCM/Li_xSi) can be regarded as the cathode-limiting system, while Case 2 (LCO/Si) is anode-limiting system. This means that prelithiation is only effective if the full-cell is anode limited.

Cells corresponding to each of these four cases were fabricated to demonstrate this hypothesis. In **Figure 5b**, which shows the NCM811 case, the ICE improvement at C/20 was marginal after prelithiation. However, the ICE of LCO cells increased significantly from 78.3% to 95.7% **(Figure 5c)**. The first-cycle voltage profile from these cells were consistent with the hypothesis illustrated in **Figure 5a**. From the rate tests in **Figure S4a** and **b**, lithiated Si always showed higher discharge capacity than non-lithiated Si for all current densities.

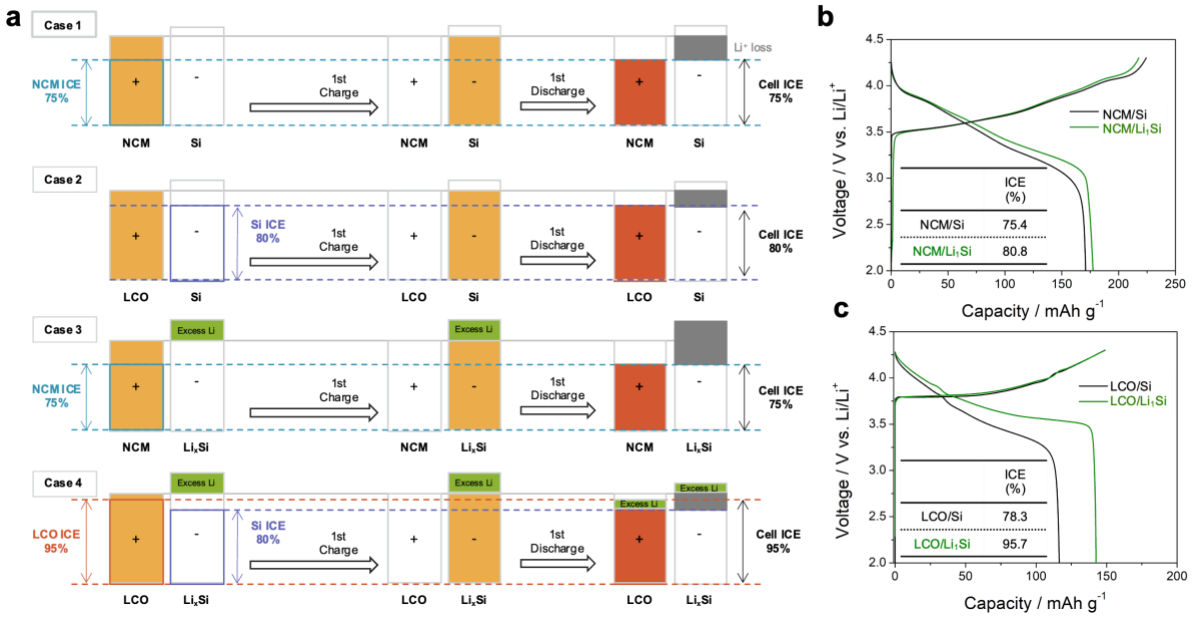

Figure 5. a) Schematic illustrating ICE estimates of the Si and Li_xSi paired with NCM and LCO cathodes. First-cycle voltage profiles of b) NCM811 and c) LCO paired with Si and Li_1Si at C/20.

2.4 Ramping test and long cycling of prelithiated Si

A ramping test using Si (**Figure 6a**) and Li_1Si (**Figure 6b**) was conducted to evaluate the lithiation effect on critical current density. Both Si and Li_1Si did not short, even up to 10 mA cm^{-2}. The areal capacities of a LCO cathode composite in all cells were 4 mAh cm^{-2}. For the first cycle at 0.25 mA cm^{-2}, both cells showed similar charge capacity suggesting good utilization of the cathode materials from the same loading. However, from the first discharge step, the difference in capacity begins to dominate, which is always higher when paired with Li_1Si. The cycling stability of both Si and Li_1Si full cells, cycled at 5 mA cm^{-2} is shown in **Figure 6c**. Even with the high rate of 1.25C (1C = 4.0 mAh cm^{-2}), the retention of Li_1Si cell was 73.8% after 1000 cycles with an average CE of 99.9%, whereas the non-lithiated Si cell demonstrated 58.7% retention after 1000 cycles. As discussed in Figure 3e, for the Si full-cell, decrease in reversible capacity originates from electrolyte decomposition at the interface (especially LPSCl/Si interface) and Li trapped in Si. Even though stabilized LPSCl/Si interface after first few cycles helps the Si full-cells to have excellent CE and cyclability, it can be clearly seen that cells with more Li inventory (excess Li by prelithiation) have better cyclability. This further supports the room temperature lithiated Si could work at high rates for extended cycling.

Interestingly, the cycling trend of lithiated Si shows an initial discharge capacity increase rather than decay. To better understand the full cells, EIS was measured for both cases upon cycling. This initial increase in discharge capacity could be attributed to residual Li metal not lithiated to Li_xSi which then becomes lithiated electrochemically in subsequent cycles. In **Figure S5**, in-situ

EIS of the full cell using both Si and Li_xSi shows a decrease in resistance as it cycles. However, the magnitude of the resistance decrease is much higher for the Li_xSi. This implies that the remaining Li in Li_xSi would keep lithiating the unlithiated Si as it cycles.

Considering the amount of Si used in the cell, all cells exhibit a high N/P ratio. The amount of Si used was fixed to 5 mg for all cells, yielding ~17.5 mAh of theoretical anode capacity and N/P ~ 4.4. The cathode loadings were further increased in **Figure S6**, from dry process LCO loading of 22 mg to 42 mg and 57 mg, each corresponding to 3.7 mAh cm^{-2}, 8.0 mAh cm^{-2} and 10.8 mAh cm^{-2} of theoretical cathode capacity. The areal capacity from three different cathode loadings corresponds well with these theoretical cathode capacities. (**Figure S7a**) The gravimetric capacity of two higher loading cells decreased by 10 mAh g^{-1}, however, even for the 10 mAh cm^{-2} cell, capacity close to theoretical capacity of LCO was achieved. This demonstrates the high capacity of lithiated Si in the full cell configuration.

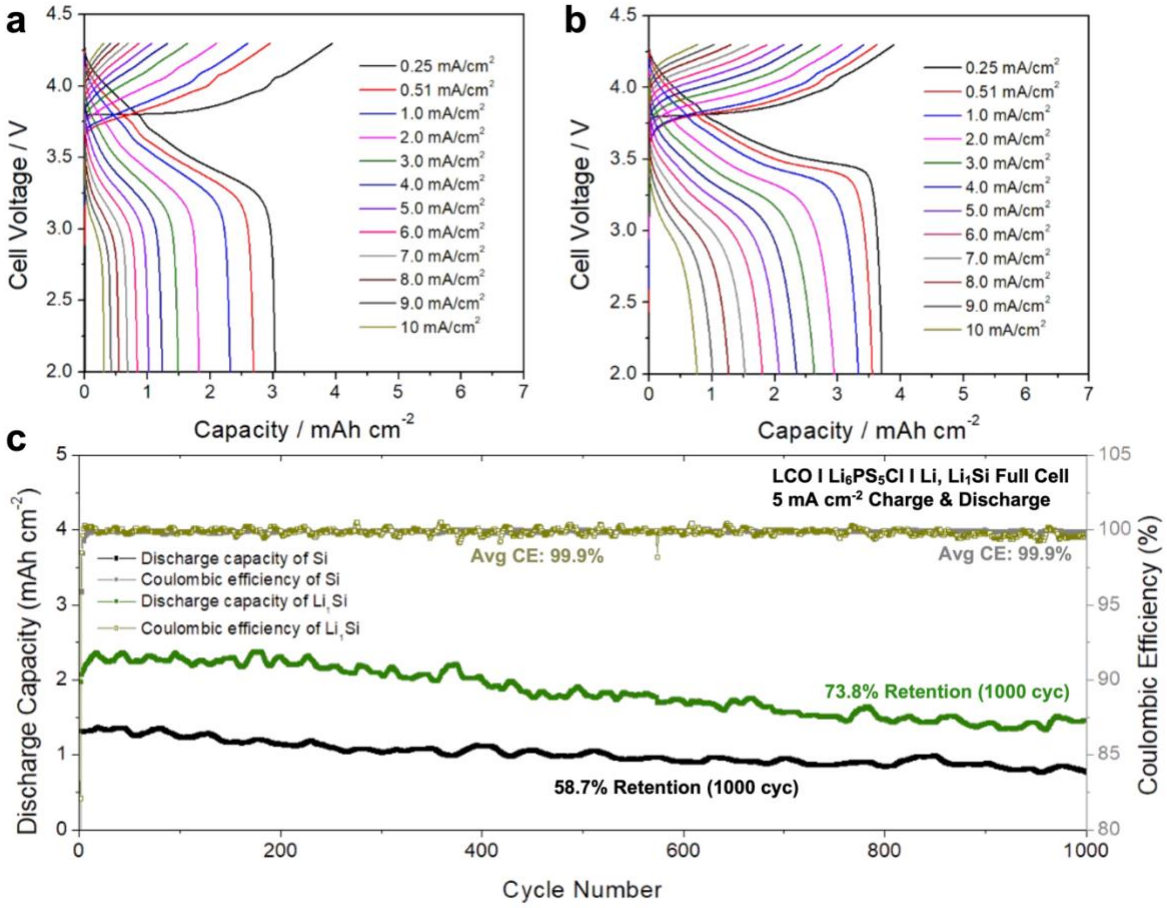

Figure 6. Ramping test to evaluate the critical current density of (a) Si and (b) Li_1Si. (c) Cycling performance of Si and Li_1Si cell at 5 mA cm^{-2}.

3. Conclusions

All-solid-state Si batteries have shown promising potential to enable high-capacity anode without continual SEI growth. However, the low ICE of Si remained a challenge to overcome for all-solid-state batteries. Here, a prelithiation strategy using the stabilized lithium was adopted to improve the ICE and conductivity of anodes. The lithiated Si was examined in symmetric-, half-, and full-cell configuration to understand the cell- level improvement of each component. With Li_1Si and LCO used as the anode and cathode, respectively, the full cell showed over 95% of ICE. In this work, we have identified why the prelithiation effect would dominate only for the anode-limited cases by comparing NCM and LCO paired with Si and Li_xSi. The ramping test and the long cycling performance were evaluated for both Si and Li_1Si cells. The Li_1Si demonstrated a large improvement of 73.8% after 1000 cycles, a 15% improvement in retention. Furthermore, using Li_1Si, high areal capacity of 10mAh cm^{-2} was achieved and demonstrated using a dry-process LCO film, demonstrating that the lithiated Si could be a suitable candidate to be used in high-energy-density next generation batteries.

Acknowledgements
This work was funded by the LG Energy Solution through Frontier Research Laboratory (FRL) program. This work was performed in part at the San Diego Nanotechnology Infrastructure (SDNI) of UCSD, a member of the National Nanotechnology Coordinated Infrastructure, which is supported by the National Science Foundation (Grant ECCS-2025752). The research reported here made use of the shared facilities of the Materials Research Science and Engineering Center (MRSEC) at UC Santa Barbara: NSF DMR-2308708. The UC Santa Barbara MRSEC is a member of the Materials Research Facilities Network (www.mrfn.com). E.S. acknowledges support from the National Science Foundation Graduate Research Fellowship under Grant NSF DGE 1650114.

Author contributions
So-Yeon Ham contributed concenptualization, data curation, methodology, formal analysis, investigation, writing – original draft, visualization. Elias Sebti contributed data curation, formal analysis, investigation, writing. Ashley Cronk contributed formal analysis, investigation. Tyler Pennebaker contributed data curation, investigation. Grayson Deysher contributed: formal analysis, validation. Yu-Ting Chen contributed investigation, visualization. Jin An Sam Oh contributed investigation, validation. Jeong Beom Lee contributed formal analysis, investigation. Min Sang Song contributed formal analysis, investigation. Phillip Ridley contributed formal analysis, investigation. Darren H. S. Tan contributed conceptualization, methodology, investigation. Raphaële J. Clément contributed formal analysis, investigation, writing. Jihyun Jang contributed conceptualization, formal analysis, writing. Ying Shirley Meng contributed conceptualization, investigation, writing.

References

1. Lewis, J. A., Cavallaro, K. A., Liu, Y. & McDowell, M. T. The promise of alloy anodes for solid-state batteries. *Joule* **6**, 1418–1430 (2022).
2. Huang, Y., Shao, B. & Han, F. Li alloy anodes for high-rate and high-areal-capacity solid-state batteries. *J. Mater. Chem. A* **10**, 12350–12358 (2022).
3. Xu, B. *et al.* Interfacial Chemistry Enables Stable Cycling of All-Solid-State Li Metal Batteries at High Current Densities. *J. Am. Chem. Soc.* **143**, 6542–6550 (2021).
4. Xiong, S. *et al.* Design of a Multifunctional Interlayer for NASCION-Based Solid-State Li Metal Batteries. *Adv. Funct. Mater.* **30**, 2001444 (2020).
5. Doux, J. *et al.* Stack Pressure Considerations for Room-Temperature All-Solid-State Lithium Metal Batteries. *Adv. Energy Mater.* **10**, 1903253 (2020).
6. Ham, S.-Y. *et al.* Assessing the critical current density of all-solid-state Li metal symmetric and full cells. *Energy Storage Materials* **55**, 455–462 (2023).
7. Lee, Y.-G. *et al.* High-energy long-cycling all-solid-state lithium metal batteries enabled by silver–carbon composite anodes. *Nat Energy* **5**, 299–308 (2020).
8. Iwamura, S. *et al.* Li-Rich Li-Si Alloy As A Lithium-Containing Negative Electrode Material Towards High Energy Lithium-Ion Batteries. *Sci Rep* **5**, 8085 (2015).
9. Wang, G. *et al.* New insights into Li diffusion in Li–Si alloys for Si anode materials: role of Si microstructures. *Nanoscale* **11**, 14042–14049 (2019).
10. Jing, W. *et al.* Li-Indium alloy anode for high-performance Li-metal batteries. *Journal of Alloys and Compounds* **924**, 166517 (2022).
11. Luo, S. *et al.* Growth of lithium-indium dendrites in all-solid-state lithium-based batteries with sulfide electrolytes. *Nat Commun* **12**, 6968 (2021).

12. Il'ina, E., Druzhinin, K., Lyalin, E. & Talankin, I. In Situ Li-In Anode Formation on the Li7La3Zr2O12 Solid Electrolyte in All-Solid-State Battery. *Batteries* **8**, 226 (2022).
13. Sedlmeier, C., Schuster, R., Schramm, C. & Gasteiger, H. A. A Micro-Reference Electrode for Electrode-Resolved Impedance and Potential Measurements in All-Solid-State Battery Pouch Cells and Its Application to the Study of Indium-Lithium Anodes. *J. Electrochem. Soc.* **170**, 030536 (2023).
14. Mou, H., Xiao, W., Miao, C., Li, R. & Yu, L. Tin and Tin Compound Materials as Anodes in Lithium-Ion and Sodium-Ion Batteries: A Review. *Front. Chem.* **8**, 141 (2020).
15. Pan, H. *et al.* Carbon-free and binder-free Li-Al alloy anode enabling an all-solid-state Li-S battery with high energy and stability. *Sci. Adv.* **8**, eabn4372 (2022).
16. Chen, S. *et al.* Aluminum−lithium alloy as a stable and reversible anode for lithium batteries. *Electrochimica Acta* **368**, 137626 (2021).
17. He, J., Wei, Y., Zhai, T. & Li, H. Antimony-based materials as promising anodes for rechargeable lithium-ion and sodium-ion batteries. *Mater. Chem. Front.* **2**, 437–455 (2018).
18. Kong, L. *et al.* Lithium–Magnesium Alloy as a Stable Anode for Lithium–Sulfur Battery. *Adv. Funct. Mater.* **29**, 1808756 (2019).
19. Zhang, C. *et al.* Challenges and Recent Progress on Silicon-Based Anode Materials for Next-Generation Lithium-Ion Batteries. *Small Structures* **2**, 2100009 (2021).
20. Zhang, X. *et al.* Stable high-capacity and high-rate silicon-based lithium battery anodes upon two-dimensional covalent encapsulation. *Nat Commun* **11**, 3826 (2020).
21. Tan, D. H. S. *et al.* Carbon-free high-loading silicon anodes enabled by sulfide solid electrolytes. *Science* **373**, 1494–1499 (2021).

22. Berhaut, C. L. *et al.* Prelithiation of silicon/graphite composite anodes: Benefits and mechanisms for long-lasting Li-Ion batteries. *Energy Storage Materials* **29**, 190–197 (2020).
23. Min, X. *et al.* Challenges of prelithiation strategies for next generation high energy lithium-ion batteries. *Energy Storage Materials* **47**, 297–318 (2022).
24. Pan, Q. *et al.* Improved electrochemical performance of micro-sized SiO-based composite anode by prelithiation of stabilized lithium metal powder. *Journal of Power Sources* **347**, 170–177 (2017).
25. Sun, C. *et al.* Recent advances in prelithiation materials and approaches for lithium-ion batteries and capacitors. *Energy Storage Materials* **32**, 497–516 (2020).
26. Yang, S.-Y. *et al.* Battery prelithiation enabled by lithium fixation on cathode. *Journal of Power Sources* **480**, 229109 (2020).
27. Liu, Q. *et al.* Understanding undesirable anode lithium plating issues in lithium-ion batteries. *RSC Adv.* **6**, 88683–88700 (2016).
28. Cao, Z. *et al.* Ambient-Air Stable Lithiated Anode for Rechargeable Li-Ion Batteries with High Energy Density. *Nano Lett.* **16**, 7235–7240 (2016).
29. Ai, G. *et al.* Scalable process for application of stabilized lithium metal powder in Li-ion batteries. *Journal of Power Sources* **309**, 33–41 (2016).
30. Forney, M. W., Ganter, M. J., Staub, J. W., Ridgley, R. D. & Landi, B. J. Prelithiation of Silicon–Carbon Nanotube Anodes for Lithium Ion Batteries by Stabilized Lithium Metal Powder (SLMP). *Nano Lett.* **13**, 4158–4163 (2013).
31. Bärmann, P. *et al.* Mechanistic Insights into the Pre-Lithiation of Silicon/Graphite Negative Electrodes in “Dry State” and After Electrolyte Addition Using Passivated Lithium Metal Powder. *Adv. Energy Mater.* **11**, 2100925 (2021).

32. Ji, W. *et al.* High-performance all-solid-state Li–S batteries enabled by an all-electrochem-active prelithiated Si anode. *Energy Storage Materials* **53**, 613–620 (2022).

33. Hope, M. A. *et al.* Selective NMR observation of the SEI–metal interface by dynamic nuclear polarisation from lithium metal. *Nat Commun* **11**, 2224 (2020).

34. R. Lide, D. in *CRC Handbook of Chemistry and Physics* Section 12, Properties of Solids; Electrical Resistivity of Pure Metals (CRC Press, 2003).

35. Gunnarsdóttir, A. B., Amanchukwu, C. V., Menkin, S. & Grey, C. P. Noninvasive *In Situ* NMR Study of "Dead Lithium" Formation and Lithium Corrosion in Full-Cell Lithium Metal Batteries. *J. Am. Chem. Soc.* **142**, 20814–20827 (2020).

36. Meyer, B. M., Leifer, N., Sakamoto, S., Greenbaum, S. G. & Grey, C. P. High Field Multinuclear NMR Investigation of the SEI Layer in Lithium Rechargeable Batteries. *Electrochem. Solid-State Lett.* **8**, A145 (2005).

37. Kim, H. J. *et al.* Controlled Prelithiation of Silicon Monoxide for High Performance Lithium-Ion Rechargeable Full Cells. *Nano Lett.* **16**, 282–288 (2016).